Layout design of a bi-stable cardiovascular stent using topology optimization

Kai A. James[a], Haim Waisman[b]

[a] *Columbia University, Department of Civil Engineering and Engineering Mechanics, New York, New York, United States; tel: 917-868-5546; fax: 212-854 -6267; kai.james@columbia.edu*

[b] *Columbia University, Department of Civil Engineering and Engineering Mechanics, New York, New York, United States*

Abstract

We present a novel design concept for a bi-stable cardiovascular stent in which the device has two fully stable, unloaded configurations: a contracted configuration used for insertion and positioning of the device, and an expanded configuration intended to facilitate blood flow. Once the device is in place, a small trigger force applied in the radial direction induces snap-through, causing the device to snap into its expanded configuration. We model the mechanics of the stent structure using a neo-Hookean hyperelastic formulation, which is discretized using a uniform mesh of solid isoparametric finite elements. Topology optimization is used to obtain the material layout and to tailor the nonlinear response of the baseline structure to achieve bi-stable snap-through behavior. The design domain is defined as a two-dimensional unit cell within the larger mesh pattern that comprises the cylindrical stent structure. We further introduce a novel transverse bracing system, which exerts a containing force that allows snap-through to occur, and that also ensures that the length of the stent does not change due to radial expansion. Optimization results are presented for several two dimensional examples including a benchmark problem based on a bi-stable beam, and a two-dimensional stent patch. Results confirm that topology optimization has been used successfully to achieve bi-stability in both the beam and the stent structures.

Keywords: topology optimization; geometric nonlinearity; cardiovascular stent design; snap-though

1. Introduction

Cardiovascular stents are meshed tubular devices that are used to prop open diseased arteries to repair and prevent blockages. These devices constitute an indispensable means of treating cardiovascular disease, and offer a minimally invasive alternative to by-pass surgery [1]. When an obstruction is identified, the mesh is inserted into the artery, and once in place, the stent is expanded in the radial direction to promote blood flow. The expansion process typically involves the use of a balloon, which is inflated to generate the outward radial force that causes the stent structure to deform in a controlled fashion. Stent design is a highly complex engineering task that must take into account a multitude of performance requirements. The various design considerations include but are not limited to stress due to tissue interaction, hemodynamic performance, mechanical behavior, and drug delivery (in the case of drug eluting stents) [2].

One of the main challenges in the design and implantation of stents is the failure of the mesh to fully expand [1, 3, 4]. This is a commonly occurring phenomenon, which is estimated to account for up to 8% of stent failures [5]. The inability to fully expand may be due to an insufficiently stiff structure, which collapses under the forced exerted by the walls of the blood vessel [3]. Alternatively, a non-uniform expansion (i.e. varying levels of expansion at different locations along the axis of the stent) due to poor layout design can cause injury to the artery, thus triggering an inflammatory response which can lead to restenosis (i.e. re-closure) of the blood vessel [6, 7]. For these reasons, it has long been understood that the clinical performance of a cardiovascular stent is highly dependent of the stent's mechanical properties [8, 9]

To address these challenges, several authors have investigated the use of computational mechanics and design optimization to create stent designs with improved mechanical properties. For example, in a 2012 study by Gundert *et al.* [10], the authors used computational fluid dynamics to design the layout of a stent mesh for optimal spatial distribution of the wall shear stress in the blood vessel, which has been linked to a variety of adverse effects including hyperplasia (inflammation) and restenosis. This study primarily addressed hemodynamic performance and fluid-structure interaction, however many others have focused on the elasto-plastic properties of the stent itself. In their 2013 study [4], Li *et al.* used a Kriging surrogate model to optimize the stent design and reduce the so-called "dogboning" effect in

which the ends of the stent expand faster and wider than the interior portion of the structure. To model the structural response, the authors used an elastic-plastic finite element model, which they implemented using the commercial software tool, ANSYS. Prior to this, Pant *et al.* implemented a multi-objective design optimization framework, which optimized recoil, tissue stresses, hemodynamic disturbance, flexibility and drug delivery [2]. Here the multi-objective optimization was carried out using a genetic algorithm and the finite element analysis was implemented using Abaqus, another commercially available software tool.

In contrast to the above-mentioned studies, Guimarães *et al.* [1]used a topology optimization approach in which they optimized the layout of a unitary patch within the stent mesh. The structural response was simulated using an elasto-plastic model implemented in ANSYS. During the expansion process, the stent structure underwent a combination of elastic and plastic strains. The objective of the optimization was to maximize the portion of the expansion, which took place in the plastic regime. In this way, the authors were able to minimize elastic recoil so that the stent would remain in its expanded configuration once deployed. The reliance on plastic expansion is typical among conventional approaches to stent design. However, the imprecision of plastic expansion can contribute to failure of the structure to fully expand, as well as potentially causing non-uniformity in the expanded stent structure.

The current study presents a novel approach, which addresses both of these challenges. The stent structures presented are designed to exhibit snap-though behavior. Each structure will have a default contracted configuration, and once the expansion force is applied, they will snap-through to a larger expanded configuration which is fully stable. In this way, we dispense with the reliance on plastic expansion, and instead rely on the the geometric nonlinearity of the design, which will naturally bias the expansion process toward the configuration of the designer's choosing. In this way, the expansion process will be more controlled and may be less susceptible to anomalies that could lead to failure or diminished performance.

Due to the snap-through functionality of these specialized stent designs, they can be treated as compliant mechanisms from a design standpoint. In recent years there have been several prominent studies highlighting the benefits of harnessing snap-through and buckling instabilities to achieve actuation as opposed to using more traditional pneumatic actuators [11]. This snap-through approach has been applied successfully in a wide range of applica-

tions from actuation of thick-walled electroactive balloons [12] to actuation of soft machines and robots [13]. Furthermore there have been many examples throughout the literature demonstrating the efficacy of topology optimization in tackling the design of actuated structures and compliant mechanisms, [14, 15, 16, 17]. Similarly, topology optimization has also been shown to be highly effective in the design of periodic materials with unique mechanical, properties, such as extreme coefficients of thermal expansion [18] and negative Poisson's ratio [19]. Many of these design principles can be leveraged in the layout design of a bi-stable stent, since the stent layout is effectively a repeating pattern of unit cells endowed with snap-through capability.

The large deformations required to achieve snap-through motion require special attention when modeling the structural response. Most topology optimization studies, even those involving compliant mechanisms, limit the structural analysis to linear elastic models. However, to accurately capture the snap-through effect, we require a hyperelastic material model. The combination of hyperelasticity with topology optimization presents some unique challenges. However, a few studies have investigated this topic, including, most recently, a study by Ramos and Paulino that looked at topology optimization of hyperelastic trusses [20]. Earlier that same year, Wallin and Ristinmaa [21] published a paper in which they addressed this issue using phase-field regularization. Also, in the previous year, Wang *et al.* [22] introduced an energy interpolation scheme for topology optimization of structures that undergo large deformations. The number of authors who have investigated topology optimization for structures exhibiting snap-through and bucking instability is even smaller still. Two notable examples are those of Bruns *et al.* [23] and Lindgaard and Dahl [24]. In the latter of these studies, the authors used geometrically nonlinear analysis based on the Total Lagrangian approach to design beams with maximal buckling load. In the former study the authors implemented a Kirchoff-St. Venant material model to design beams that intentionally exhibited snap-through instability.

Both of the above-mentioned studies limited their examples to beam problems. In the current study we devise and implement unique boundary conditions necessary to achieve snap-through and bi-stability in a unitary cell within the larger stent mesh, and we address the various numerical and design challenges that arise due to the unique geometry of the problem. The geometrically non-linear finite element analysis is implemented using a Neo-Hookean material model, and solved iteratively using the arc-length method. We present two distinct examples of stent designs, obtained using the pro-

posed optimization algorithm, and provide discussion and analysis of the merits of each design. The remainder of the paper is organized as follows. In Section 2 we present the theoretical framework and methodology used to solve the structural analysis problem, while accounting for large deformations. In the following section (3) we provide an overview of the topology optimization problem, and give a breakdown of the various components of the optimization algorithm and the role of each in the larger design task. In this section we provide an outline of the gradient-based optimization algorithm, and a description of the adjoint sensitivity analysis calculation. In Section 4 we present the problem specifications and numerical results, along with analysis and discussion of several example problems. Lastly, in Section 5, we summarize and draw conclusions based on our findings.

2. Large Deformation Modeling

2.1. Kinematics and Equilibrium

Central to the design optimization task, is the ability to accurately and efficiently model the structural response of the various candidate designs that arise over the course of the optimization search. Before addressing the mechanics of the analysis problem, we require a system for describing the geometry and motion of the structure as it undergoes large deformations. The following section contains definitions of the various terms and quantities required to capture the kinematics of the structural analysis problem. The derivations that follow are based primarily on the work presented by Belytschko *et al.* [25], and are included here for completeness.

Given a material subject to large deformations, we assumed a continuous mapping between coordinates in the undeformed state, $\mathbf{X}$, and coordinates in the current (deformed) state, $\mathbf{x}$. We therefore, define the deformation gradient, $\mathbf{F}$, as follows.

$$\mathbf{F} = \frac{\partial \mathbf{x}}{\partial \mathbf{X}} \tag{1}$$

Given a displacement state $\mathbf{u}$ and noting that $\mathbf{x} = \mathbf{X} + \mathbf{u}$, we can also express the deformation gradient in terms of the displacement state as follows.

$$\mathbf{F} = \left(\frac{\partial \mathbf{X}}{\partial \mathbf{x}}\right)^{-1} = \left(\mathbf{I} - \frac{\partial \boldsymbol{u}}{\partial \mathbf{x}}\right)^{-1} \tag{2}$$

where $\mathbf{I}$ is the identity tensor. We define an additional quantity, $\mathbf{C}$, which is referred to as the right Cauchy-Green tensor, and is given by

$$\mathbf{C} = \mathbf{F}^{\mathrm{T}}\mathbf{F}. \tag{3}$$

Similarly, the left Cauchy-Green tensor is defined as

$$\mathbf{B} = \mathbf{F}\mathbf{F}^{\mathrm{T}}. \tag{4}$$

Lastly, we define the relevant strain tensor, in this case the Green-Lagrange strain, $\mathbf{E}$, using

$$\mathbf{E} = \frac{1}{2}\left(\mathbf{C} - \mathbf{I}\right). \tag{5}$$

To solve the mechanics problem, we use a compressible Neo Hookean constitutive model [25]. For a material having Lamé constants, λ_0 and μ_0[1], The total potential energy function is given by

$$\Phi = \frac{1}{2}\lambda_0[\ln J]^2 - \mu_0 \ln J + \frac{1}{2}\mu_0[\mathrm{tr}(\mathbf{C}) - 3] \tag{6}$$

where J is computed as $\det(\mathbf{F})$. Note that symbol $\mathrm{tr}(*)$ denotes the trace operator. From here, we can compute the Second Piola-Kirchoff stress, $\mathbf{S}$, which relates the forces in the reference configuration with areas also measured in the reference configuration.

$$\mathbf{S} = 2\frac{\partial \Phi}{\partial \mathbf{C}} \tag{7}$$

$$= \lambda_0[\ln J]\mathbf{C}^{-1} + \mu_0\left(\mathbf{I} - \mathbf{C}^{-1}\right), \tag{8}$$

Using the Second Piola-Kirchoff stress, we can evaluate the Cauchy stress, $\boldsymbol{\sigma}$, which relates forces in the deformed configuration with areas in the deformed configuration. This quantity is computed as follows.

[1]Note that the Lamé parameters can be expressed in terms of the Young's modulus, E and the Poisson's ratio, ν using $\mu_0 = \frac{E}{2(1+\nu)}$ and $\lambda_0 = \frac{\nu E}{(1+\nu)(1-2\nu)}$

$$\boldsymbol{\sigma} = \frac{1}{J}\mathbf{F}\mathbf{S}\mathbf{F}^{\mathrm{T}} \tag{9}$$

Combining equations 8 and 9 one can derive the following expression for the Cauchy stress.

$$\boldsymbol{\sigma} = \frac{1}{J}\left[\lambda_0[\ln J]\mathbf{I} + \mu_0\left(\mathbf{F}\mathbf{F}^{\mathrm{T}} - \mathbf{I}\right)\right] \tag{10}$$

$$= \frac{1}{J}\left[\lambda_0[\ln J]\mathbf{I} + \mu_0\left(\mathbf{B} - \mathbf{I}\right)\right] \tag{11}$$

2.2. Finite Element Discretization

We compute the displacement field of the structure by solving the equilibrium equations throughout its volume. For a volume element occupying the domain Ω subject to body forces $\boldsymbol{b}$ and surface tractions $\boldsymbol{t}$, the strong form of the governing equilibrium equations expressed in the current (deformed) configuration are shown below.

$$\begin{aligned} \frac{\partial \boldsymbol{\sigma}}{\partial \mathbf{x}} + \boldsymbol{b} &= 0 \ \text{ in } \Omega \\ \boldsymbol{\sigma}\boldsymbol{n} &= \boldsymbol{t} \ \text{ on } \Gamma_N \\ \boldsymbol{u} &= 0 \ \text{ on } \Gamma_D \end{aligned} \tag{12}$$

Here, as in the previous subsection, $\boldsymbol{\sigma}$ denotes the Cauchy stress tensor, while $\mathbf{x}$ denotes the current coordinates. Note also that Γ_N and Γ_D, represent Dirichlet and Neumann boundary conditions respectively, and $\boldsymbol{n}$ denotes the unit vector normal to the surface $\partial\Omega$. By discretizing the domain using finite elements, and solving the governing equations on each element, we are able to obtain accurate predictions of the displacement field for structures having non-trivial geometries. Note that in accordance with the updated Lagrangian approach, the discrete equations are formulated in terms of the current (deformed) configuration.

When the elasticity problem is discretized using finite elements, the deformation gradient can be written in terms of the element nodal displacement vector $\bar{\boldsymbol{u}}_e$, as follows

$$\mathbf{F} = \left(\mathbf{I} - \bar{\mathbf{B}}^{\mathrm{T}} \bar{\boldsymbol{u}}_e\right)^{-1} \tag{13}$$

Here, $\bar{\mathbf{B}}$ is the strain-displacement matrix, which contains the spatial derivatives of the finite element shape functions $\bar{\mathbf{N}}$, differentiated with respect to the deformed coordinates, such that

$$\bar{\mathbf{B}} = \frac{\partial \bar{\mathbf{N}}}{\partial \mathbf{x}}. \tag{14}$$

Note that, in the above notation, the bar ($\bar{*}$) signifies a matrix associated with the discrete finite element problem, whereas simple boldface signifies a vector or tensor in three-dimensional space. For a given element, e, the vector of internal nodal forces is given by

$$\bar{\boldsymbol{f}}_{\mathrm{int},e} = \int_{\Omega_e} \bar{\mathbf{B}}^{\mathrm{T}} \bar{\boldsymbol{\sigma}} \mathrm{d}\Omega_e, \tag{15}$$

where $\bar{\boldsymbol{\sigma}}$ signifies the stress tensor written in Voigt notation as a 6×1 (in three dimensions) or a 3×1 (in two dimensions) matrix. Similarly, the vector of external nodal forces is given by

$$\bar{\boldsymbol{f}}_{\mathrm{ext},e} = \int_{\Omega_e} \bar{\mathbf{N}}^{\mathrm{T}} \boldsymbol{b} \mathrm{d}\Omega_e + \int_{\Gamma_{\mathrm{N}}} \bar{\mathbf{N}}^{\mathrm{T}} \boldsymbol{t} \mathrm{d}\Gamma_{\mathrm{N}e}, \tag{16}$$

where, as before, $\boldsymbol{b}$ and $\boldsymbol{t}$ denote the distribution of body forces and surface tractions respectively.

For a finite element model containing n elements, we can assemble the element force vectors and element stiffness matrices into their global counterparts using

$$\bar{\boldsymbol{F}} = \mathcal{A}_{e=1}^{n} \bar{\boldsymbol{f}}_e; \quad \bar{\boldsymbol{K}} = \mathcal{A}_{e=1}^{n} \bar{\boldsymbol{k}}_e \tag{17}$$

where the assembly operator $\mathcal{A}$ implies a summation of all elements' respective contributions to shared degrees of freedom within the global system.

From the equilibrium of the structure, we know that the internal forces must be balanced by the external forces. Therefore, we can write the global governing equation in residual form as follows.

$$\bar{\boldsymbol{R}} = \bar{\boldsymbol{F}}_{\text{ext}} - \bar{\boldsymbol{F}}_{\text{int}} = \boldsymbol{0} \tag{18}$$

The resulting global residual represents a nonlinear system of equations, which are solved iteratively using a Newton–Raphson procedure to obtain the global vector of nodal displacements, $\bar{\boldsymbol{u}}$. Accordingly, during each iteration, one solves the following linear algebraic equation to obtain an update, $\Delta\bar{\boldsymbol{u}}$.

$$\bar{\boldsymbol{K}}_{\text{tan}}\Delta\bar{\boldsymbol{u}} = \bar{\boldsymbol{R}} \tag{19}$$

Here $\bar{\boldsymbol{K}}_{\text{tan}}$ represents the Jacobian or *tangent stiffness matrix*, which results from global assemblage of the element stiffness matrices, $\bar{\boldsymbol{k}}_{\text{tan},e}$. Following the convention used in [26], the element tangent stiffness matrix is decomposed into a geometric and a material component such that $\bar{\boldsymbol{k}}_{\text{tan},e} = \bar{\boldsymbol{k}}^{\text{geo}}_{\text{tan},e} + \bar{\boldsymbol{k}}^{\text{mat}}_{\text{tan},e}$. Prior to being assembled, the two components of the element tangent stiffness matrix are computed in terms of the Cauchy stress tensor, $\boldsymbol{\sigma}$, and constitutive tensor, $\bar{\mathbf{D}}$, expressed in Voigt matrix form such that

$$\bar{\mathbf{D}} = \begin{bmatrix} \lambda_0 + 2\mu_0 & \lambda_0 & 0 \\ \lambda_0 & \lambda_0 + 2\mu_0 & 0 \\ 0 & 0 & \mu_0 \end{bmatrix}. \tag{20}$$

The components of the tangent stiffness matrix can then be computed using

$$\bar{\boldsymbol{k}}^{\text{mat}}_{\text{tan},e} = \int_{\Omega_e} \bar{\mathbf{B}}^{\mathrm{T}}\bar{\mathbf{D}}\bar{\mathbf{B}}\mathrm{d}\Omega_e \tag{21}$$

$$\bar{\boldsymbol{k}}^{\text{geo}}_{\text{tan},e} = \mathbf{I}_{\mathrm{d}\times\mathrm{d}} \otimes \left(\int_{\Omega_e} \tilde{\mathbf{B}}^{\mathrm{T}}\boldsymbol{\sigma}\tilde{\mathbf{B}}\mathrm{d}\Omega_e \right). \tag{22}$$

Here $\mathbf{I}_{\mathrm{d}\times\mathrm{d}}$ represents the 2×2 or 3×3 identity matrix, depending on whether the problem is being solved in two or three dimensions. Note also that $\otimes$

represents the matrix outer product, and $\tilde{\mathbf{B}}$ symbolizes a special compact version of the strain displacement matrix, which retains only the nonzero entries from the original matrix, $\bar{\mathbf{B}}$. In the case of a 4-node quadrilateral element, $\tilde{\mathbf{B}}$, is computed as

$$\tilde{\mathbf{B}} = \begin{bmatrix} \bar{B}_{1,1} & \bar{B}_{1,3} & \bar{B}_{1,5} & \bar{B}_{1,7} \\ \bar{B}_{2,2} & \bar{B}_{2,4} & \bar{B}_{2,6} & \bar{B}_{2,8} \end{bmatrix}. \tag{23}$$

Due to the nonlinearity of the problem, the governing equation ($\boldsymbol{R} = \mathbf{0}$) is solved using a combination of the arc-length method and displacement control, following the procedure used by Bruns *et al.* [14]. The algorithm proceeds initially as an arc-length procedure, until the displacement at the designated degree of freedom exceeds the target value, at which point we switch to displacement-control. The result is a de facto displacement-control algorithm that is able to converge in the presence of both snap-through and snap-back. Using this approach, we solve the global residual equation to obtain both the displacement state, $\boldsymbol{u}$, and the magnitude of the external force θ, where

$$\bar{\boldsymbol{F}}_{\text{ext}} = \theta \hat{\boldsymbol{F}}_{\text{ext}}. \tag{24}$$

Here, $\hat{\boldsymbol{F}}_{\text{ext}}$ is a reference force vector of unit magnitude that describes the direction and location of the external force, while θ is a scalar that captures the force intensity. In the forward analysis problem, θ replaces the fixed displacement, u_i, corresponding to the i^{th} degree of freedom, whose value is assigned during the displacement control procedure. We can therefore express the unknown state vector as $\tilde{\boldsymbol{u}}$, where $\tilde{\boldsymbol{u}}$ is simply the global displacement vector with the i^{th} entry having been replaced with θ. Readers are encouraged to consult Bruns *et al.* [23] for a detailed description of the iterative solution procedure.

3. Structural Design Via Topology Optimization

The topology optimization method approaches the design task as a material distribution problem. We begin by defining a working domain, Δ, which represents a fixed region in physical space, within which we shall distribute material to produce some optimal structure. The domain, Δ, is a bounded

set in d-dimensional space ($\Re^d$, with $d \in \{2, 3\}$), which contains all admissible shapes Ω. The variable Ω represents the material domain which determines the structural layout of the design as illustrated in Figure 1. The material boundary is represented by $\partial\Omega$ and contains both the Dirichlet and Neumann domains (i.e. $\Gamma_D \cup \Gamma_N \subset \partial\Omega$).

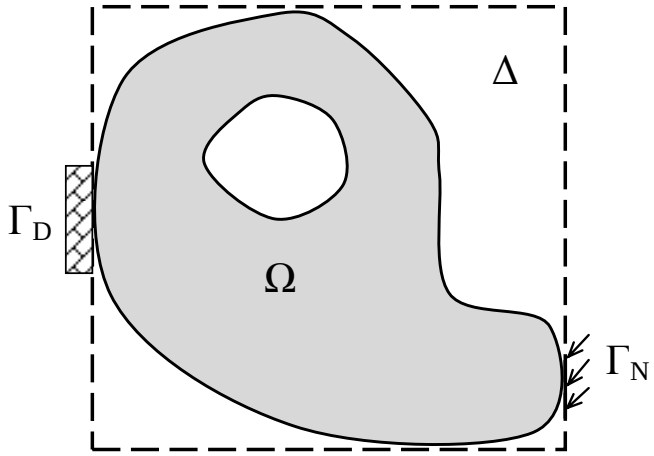

Figure 1: Topology optimization as a material distribution problem, with surface traction and fixed boundary conditions

Using numerical optimization we seek to minimize an objective function $f_o(\boldsymbol{u}, \Omega)$, which will depend on the displacement state, $\boldsymbol{u}$, of the structure, and may also have some direct dependence on Ω. The problem can be written in mathematical form as follows.

$$\begin{aligned} \min_{\Omega} \quad & f_o(\boldsymbol{u}, \Omega) \\ \text{subject to:} \quad & c_i(\boldsymbol{u}) \geq 0, \ i = 1, 2, ...n_i \\ & \tilde{c}_j(\boldsymbol{u}) = 0, \ j = 1, 2, ...n_e \end{aligned} \tag{25}$$

Here $\{\tilde{c}_i\}$ and $\{c_j\}$ represent the equality and inequality constraints respectively. Examples of typical constraints used in structural optimization problems include mass, total strain energy, and maximum local stress.. This task can be interpreted as an *inverse* problem in which one must find the structure, Ω^*, that generates the desired structural response (i.e. that which satisfies the condition $f_o(\Omega^*, \boldsymbol{u}(\Omega^*)) = \min\{f_o\}$). This is in contrast to the

forward problem, where, for a given structure, Ω, we must determine the corresponding structural response, $\boldsymbol{u}$. The forward analysis requires us to solve the nonlinear governing equations which, in this case, are based on finite strain theory with a Neo-Hookean material model. As the algorithm traverses the design space, the solution of the forward problem is used to guide the optimization search at each point in the search path. Section 3 contains a detailed description of the analytical framework used to solve the nonlinear mechanics problem, while Section 4 describes the gradient-based procedure used to solve the inverse problem.

3.1. Design Parameterization

The first step in the solution of the optimization problem described in Eqn. 25, is to discretize the working domain using finite elements. From here, the design problem can be parameterized by determining which elements should be contained within the material region, and which should be excluded. In the current study, we carry out this task using the SIMP (*solid isotropic material with penalization*) method [27, 28]. In this gradient-based approach, the design is represented by a set of material densities $\rho \in [0, 1]$, which determine the effective elasticity modulus, E_e, at a given location within the working domain via the equation

$$E_e = E_{min} + \rho^p (E_0 - E_{min}), \tag{26}$$

where, E_0 is the Young's modulus of the solid material, E_{min} is a small non-zero quantity, which serves as a lower bound for the effective elasticity modulus, and p is the SIMP penalization parameter. Optimization is used to determine the optimal values of each element's density, with $\rho = 0$ representing the void region, and $\rho = 1$ representing the material region. The penalization factor is assigned a value satisfying $p > 1$, so that intermediate densities are penalized and the algorithm converges to a 0-1 solution, which provides a mosaic-like representation of the optimized structure. We use an element-based formulation in which each element has its own density variable, so that the density field is treated as piecewise constant in each element. In the current study, E_{min} is chosen such that $E_{min}/E_0 = 2.5 \times 10^{-3}$. In this way, elements with zero material density (i.e. $E_e = E_{min}$) effectively mimic the mechanical behavior of void space by contributing only a small amount of stiffness to the overall structure. In standard SIMP-based schemes, the

enforcement of a lower bound, $E_{min} > 0$, is required to prevent singularities in the global stiffness matrix. However, in problems involving large deformations, allowing the element stiffness to become too small, can lead to severe mesh distortions and the emergence of degenerate elements [23]. Therefore the lower bound used in this study is slightly greater than that which is typically used with linear elastic material models.

The finite element analysis is performed using first-order isoparametric elements. However, it is well-known that the combination of the element-based formulation, with first-order elements can cause mesh-dependence and checkerboarding [29, 30] unless steps are taken to mitigate these phenomena. To address both issues, we implement the density filtering technique introduced by Bruns and Tortorelli [14]. For a problem involving n finite elements, and n unique material densities, we define an auxiliary vector of independent variables, $\boldsymbol{s} \in [0,1]^n$. This variable $\boldsymbol{s}$, can be interpreted as a set of pseudo-densities, which fully describe the density field via the following relationship.

$$\rho_i = \frac{\sum_{j \in \Omega_i} w_{ij}(r_{ij}) s_j}{\sum_{j \in \Omega_i} w_{ij}(r_{ij})} \tag{27}$$

Here the density, ρ_i, of element i is a weighted sum of the pseudo-densities s_j of all elements, j, within a prescribed neighborhood, Ω_i. The weighting coefficients, w_{ij}, can be chosen as any decreasing function of the distance, r_{ij}, between the centroids of the two elements (i.e. $r_{ij} = ||\mathbf{X}_i - \mathbf{X}_j||$). In the current study we use a linear function, Φ, so that

$$w_{ij} = \Phi(r_{ij}) = \max\{0, r_f - r_{ij}\} \tag{28}$$

where r_f is the filter radius. This formulation couples the densities of all elements within a radius r_f, and the filter radius is used to control the length scale of the features within the optimized structure. In addition to providing control over the size of the structural features, the density filter eliminates checkerboarding and ensures that the layout of the optimized structure is independent of the finite element discretization [14, 31].

In the optimization problem, the pseudo-densities, $\boldsymbol{s}$, serve as the independent variables, which are directly modified by the optimizer, while the densities, $\boldsymbol{\rho}$, constitute a set of physical variables, which are used to construct the global stiffness matrix of the structure via Equation 26. Note that in Equation 27, the denominator is used simply to normalize the weights. Therefore, for notational brevity, we define the set of normalized weights, $\{\hat{w}_{ij}\}$, as

$$\hat{w}_{ij} = \frac{w_{ij}}{\sum_{j \in \Omega_i} w_{ij}}. \tag{29}$$

Now, given a set of pseudo-densities, $\boldsymbol{s}$, we can apply the density filter using

$$\boldsymbol{\rho} = \hat{\boldsymbol{W}} \boldsymbol{s}, \tag{30}$$

where $\hat{\boldsymbol{W}}$, is the matrix of normalized weight coefficients, $\{\hat{w}_{ij}\}$. This matrix needs to be computed only once at the beginning of the optimization procedure, and stored so that the filter can be applied during each iteration.

3.2. Sensitivity Analysis

Due to the large number of design variables required to obtain a sufficiently well-refined optimized design, gradient-based methods are required for the solution of the nonlinear programming problem [32]. In this class of optimization methods, the search for the optimal design takes place along a single path whose trajectory is determined by the gradients of the objective and constraint functions. In the current study, these gradients are evaluated analytically using the adjoint method. Below we derive the adjoint formulation corresponding to the elasticity model described in Section 3. (Note that for notational clarity, in this and all subsequent sections we dispense with the bar accents ($\bar{*}$), since all boldface quantities that follow will refer to vectors and matrices corresponding to the finite element discretization of the problem, and not to vectors in three-dimensional space.

The governing equilibrium equation can be expressed in residual form as follows.

$$\boldsymbol{R} = \boldsymbol{F}_{\text{int}} - \theta \boldsymbol{F}_{\text{ext}} = \boldsymbol{0}, \tag{31}$$

For a given function of interest, f, which can represent either the objective or a constraint function, we express the function in the form of an augmented Lagrangian, g, such that

$$g = f + \boldsymbol{\psi}^{\mathrm{T}} \boldsymbol{R}, \tag{32}$$

where $\boldsymbol{\psi}$ is a Lagrange multiplier, whose value will be determined later. Note that $g = f$ for all $\boldsymbol{\psi}$, since $\boldsymbol{R}$ is identically zero. Therefore finding the value of the derivative $\frac{\partial g}{\partial \boldsymbol{\rho}}$, yields the sensitivities of the function f with respect to the element material densities $\boldsymbol{\rho}$. Using the chain rule, we can obtain a general expression for the derivative of g as follows.

$$\frac{\partial g}{\partial \boldsymbol{\rho}} = \frac{\partial f}{\partial \boldsymbol{\rho}} + \frac{\partial f}{\partial \tilde{\boldsymbol{u}}} \frac{\mathrm{d}\tilde{\boldsymbol{u}}}{\mathrm{d}\boldsymbol{\rho}} + \boldsymbol{\psi}^{\mathrm{T}} \left[\frac{\partial \boldsymbol{R}}{\partial \boldsymbol{\rho}} + \frac{\partial \boldsymbol{R}}{\partial \tilde{\boldsymbol{u}}} \frac{\mathrm{d}\tilde{\boldsymbol{u}}}{\mathrm{d}\boldsymbol{\rho}} \right] \tag{33}$$

Here, the operator $\frac{\partial}{\partial \boldsymbol{\rho}}$ represents an explicit derivative, which captures only the direct dependence of a function with respect to $\boldsymbol{\rho}$, while the operator $\frac{\mathrm{d}}{\mathrm{d}\boldsymbol{\rho}}$ symbolizes the *implicit* derivative, which is so named because it conveys any indirect dependence a function has with respect to $\boldsymbol{\rho}$, due to the solution of the residual equation, when solved for the state variable $\tilde{\boldsymbol{u}}$. The sum of the implicit and explicit terms is hereafter referred to as the *total* derivative. Because the implicit derivative is computationally expensive to evaluate [33, 34], we seek a solution of the Lagrange multiplier $\boldsymbol{\psi}$, which causes all implicit terms to vanish.

Re-arranging Eqn. 33 to group all implicit terms, we obtain

$$\frac{\partial g}{\partial \boldsymbol{\rho}} = \frac{\partial f}{\partial \boldsymbol{\rho}} + \boldsymbol{\psi}^{\mathrm{T}} \frac{\partial \boldsymbol{R}}{\partial \boldsymbol{\rho}} + \left[\frac{\partial f}{\partial \tilde{\boldsymbol{u}}} + \boldsymbol{\psi}^{\mathrm{T}} \frac{\partial \boldsymbol{R}}{\partial \tilde{\boldsymbol{u}}} \right] \frac{\mathrm{d}\tilde{\boldsymbol{u}}}{\mathrm{d}\boldsymbol{\rho}} \tag{34}$$

From here, it is clear that by setting the $\boldsymbol{\psi}$ such that

$$\boldsymbol{\psi} = - \left[\frac{\partial \boldsymbol{R}}{\partial \tilde{\boldsymbol{u}}} \right]^{-\mathrm{T}} \frac{\partial f}{\partial \tilde{\boldsymbol{u}}}^{\mathrm{T}} = \tilde{\boldsymbol{K}}_{\mathrm{tan}}^{-\mathrm{T}} \frac{\partial f}{\partial \tilde{\boldsymbol{u}}}^{\mathrm{T}}, \tag{35}$$

all implicit terms drop out (note that in the above equation, we have made use of the fact that $\frac{\partial \boldsymbol{R}}{\partial \tilde{\boldsymbol{u}}}$ is equal to the tangent stiffness matrix $\tilde{\boldsymbol{K}}_{\mathrm{tan}}$). When

chosen in this way, the parameter $\boldsymbol{\psi}$ is known as the *adjoint* state or adjoint vector. When the adjoint vector is substituted into Eqn. 33, the total derivative reduces to

$$\frac{\partial g}{\partial \boldsymbol{\rho}} = \frac{\partial f}{\partial \boldsymbol{\rho}} + \boldsymbol{\psi}^{\mathrm{T}} \frac{\partial \boldsymbol{R}}{\partial \boldsymbol{\rho}} \tag{36}$$

To account for the density filtering process described in Section 3.1, we again invoke the chain rule, by noting that

$$\frac{\partial g}{\partial \boldsymbol{s}} = \frac{\partial g}{\partial \boldsymbol{\rho}} \frac{\partial \boldsymbol{\rho}}{\partial \boldsymbol{s}} = \frac{\partial g}{\partial \boldsymbol{\rho}} \hat{\boldsymbol{W}} \tag{37}$$

3.3. Algorithm Summary

The optimization problem is solved computationally using the Method of Moving Asymptotes [35]. Similar to sequential quadratic programming, during each optimization iteration, the algorithm constructs and solves a convex approximation of the problem based on the current value and gradients of the Lagrangian. Figure 2 contains a schematic illustration of the overall algorithm, including both the forward analysis problem, and the sensitivity analysis. The solution of the convex subproblem then becomes the updated design point in the optimization search. The algorithm terminates when the first order Karush-Kuhn-Tucker conditions are satisfied [36, 37].

4. Numerical Examples

In order to achieve the desired snap-through behavior in the optimized stent designs, we use optimization to tailor the nonlinear response of the structure. The force-displacement curves shown in Fig. 3 illustrate how the response curve of the structure is progressively modified over the course of the optimization. In the figure, it is shown that through optimization, one can push the force-displacement profile downward so that it dips below the x-axis, which signifies that a bi-stable snap-through response has been achieved. In the examples that follow, the objective is to minimize the externally applied force, θ_2 at the prescribed displacement point u_2, subject to a constraint on the applied force θ_1 at some earlier displacement point, u_1, such that $\theta(u_1) \geq F_{\min}$, where $F_{\min} > 0$. A formal statement of the optimization problem is given below.

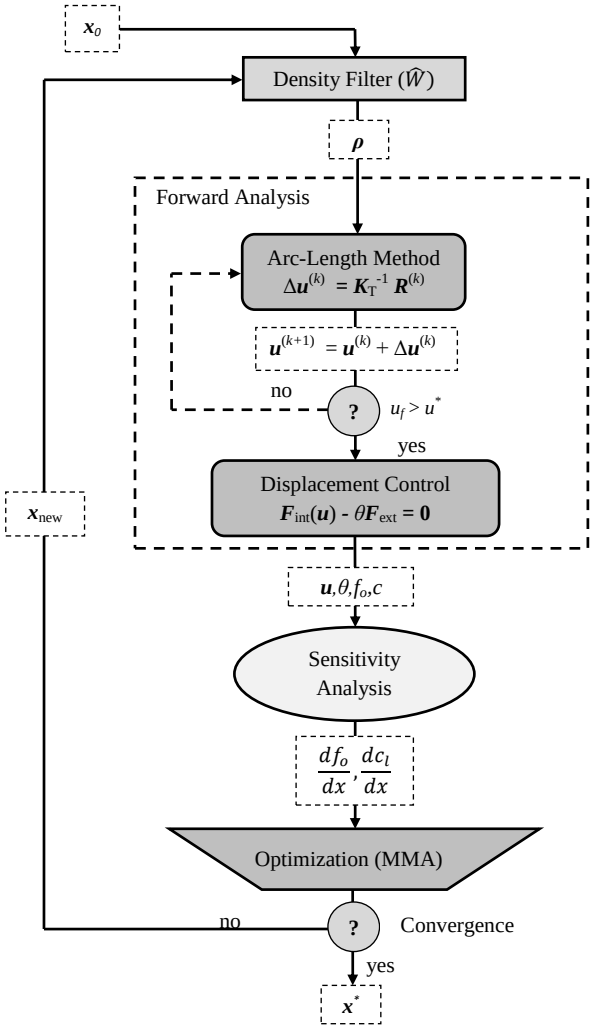

Figure 2: Sequence of operations and data flow during the design optimization algorithm

$$\begin{aligned} \min_{\boldsymbol{x}} \quad & \theta_2 \\ \text{subject to:} \quad & \theta_1 \geq F_{\min} \\ & M(\boldsymbol{s}) \leq M_{\max} \end{aligned} \tag{38}$$

Note that in 38, M represents the total mass of the structure. An addi-

tional constraint on the maximum allowable mass is enforced to avoid the unnecessary inclusion of excess material. Note that if this mass constraint is omitted, then the optimizer will leave superfluous material that confers little or no mechanical advantage. Therefore, in each of the examples presented, the mass constraint has been chosen so that it eliminates useless material, without excessively impeding the optimization search.

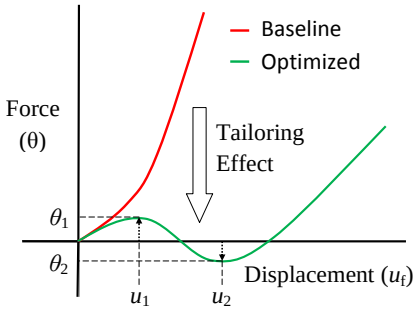

Figure 3: Sample force-displacement curves for baseline and optimized structures

By requiring some requisite stiffness at the point u_1, we ensure that the optimizer does not minimize θ_2 by simply producing the weakest structure possible, as this would constitute an unsatisfactory local minimum. If the algorithm manages to find a solution to problem 38, in which $\theta_2 < \theta_1$, then the corresponding structure will exhibit snap-through. For solutions in which $\theta_2 < 0$ the design will be bi-stable. From the shape of the green force-displacement curve in Fig. 3, one can observe that a lower value of θ_2 (i.e. a larger magnitude for the negative applied force) leads to a larger expansion at the second stable equilibrium point (i.e. the rightmost point at which the curve traverses the x-axis). This implies a higher expansion ratio for the stent structure between its expanded and contracted configurations. More importantly, a lower value for θ_2, translates to increased stiffness for the structure while in its expanded configuration. (Here, the stiffness at the second stable equilibrium point is given by the slope of the force-displacement curve at the rightmost x-intercept). Therefore, θ_2 is a suitable choice for the objective function in the optimization of the bi-stable stent structure. Note that we are able to achieve snap-through by evaluating the response of the structure at just two points along the load path, and by constraining the structural response at just one point. In this way, we avoid over-designing the struc-

ture, and allow the algorithm to determine the optimal force-displacement response for the specified design objective. It should also be noted that the displacement points u_1 and u_2 may not necessarily correspond to local extrema withing the force-displacement plot, and in practice, this will rarely be the case.

4.1. The Bi-Stable Beam

Before delving into the stent design task, we begin with a classic problem involving snap-through instability. In order to gain further insight into the mechanics of the snap-through phenomenon and to validate both the elasticity model and the optimization strategy, we first optimize a beam structure, which is clamped at both ends and subject to a transverse point load. Figure 4 shows the geometry and boundary conditions of the working domain for the beam structure. The baseline structure (i.e. the fully solid layout in which no elements have been removed), is not bi-stable. Therefore, using the optimization algorithm described in the previous sections, we seek to redistribute material within the prescribed domain to generate a bistable beam structure.

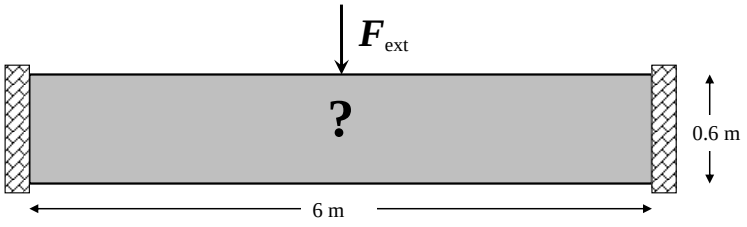

Figure 4: Geometry and boundary conditions for the bi-stable beam problem (note that the beam has a uniform thickness of 0.1m)

The beam material has a Young's modulus $E = 15 \times 10^6$Pa, and a Poisson's ratio $\nu = 0.3$. The designated displacement points for the optimization are $u_1 = 0.225$cm and $u_2 = 0.65$cm, and the stiffness constraint is chosen so that $\theta_1 \geq 620$N (note that for this problem, downward forces and displacements are assumed to be positive). To avoid local minima, we employ a continuation method [38] in which the the SIMP penalization parameter, p, is assigned based an increasing step function of the iteration number, j, such that

$$p(j) = \min\{1.0, \max\{\lceil j/5 \rceil, 3.0\}\}, \quad \text{for} \quad j = 1, 2, ... \tag{39}$$

where the operator $\lceil * \rceil$ indicates that the enclosed quantity is rounded up to the nearest integer value. In this way, the optimization starts out with no penalization of intermediate densities (i.e. $p = 1$), and after every 5 iterations, the penalization parameter is increased by 1 until it reaches a maximum value of $p = 3$.

Figure 7 shows the optimized design for the bi-stable beam in each of its two equilibrium positions. Note that the structure contains three narrow joints that act as flexural hinges, about which rotational motion takes place. As indicated by the von Mises stress distribution shown in Fig. 6, the majority of the stress in the structure is concentrated at these locations.

(a) Configuration #1 (b) Configuration #2

Figure 5: Optimized material layout for the bi-stable beam structure

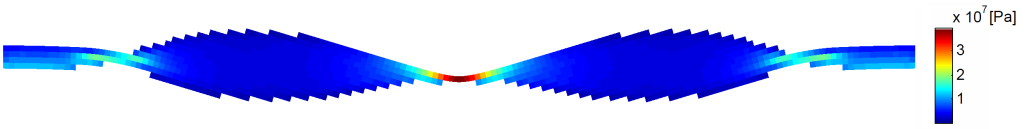

Figure 6: The von Mises stress distribution in the bi-stable bar while in its secondary equilibrium state

Figure 5 shows the force-displacement curves for the baseline beam structure and the optimized, bi-stable beam. In the plot on the right, the first red marker indicates the target force value specified through the stiffness constraint and evaluated at the designated displacement point u_1. The second red marker indicates the value of the objective function evaluated at the designated displacement point u_2. The plots confirm that the optimization procedure has succeeded in achieving bi-stability, as the force-displacement curve of the optimized beam dips below the x-axis when the deflection exceeds the limit point of 0.59m.

The portion of the force-displacement plot for deflections within the range (0m, 0.59m) corresponds to the initial displacement of the beam, during which time it resists the applied force by pushing back with an equal and opposite internal force. For this reason, the force values in this region of the plot are all positive. Once the deflection passes the limit point of 0.59m, the internal forces within the beam are reversed, and the beam naturally snaps through to its secondary equilibrium position at 0.82m. To hold the beam in equilibrium at deflections between 0.59m and 0.82m, one must apply a negative external force (in this case, an upward force), whose magnitude is indicated by the path of the plot within this domain. This force reversal is characteristic of snap-through behavior, and is what makes the structure bi-stable.

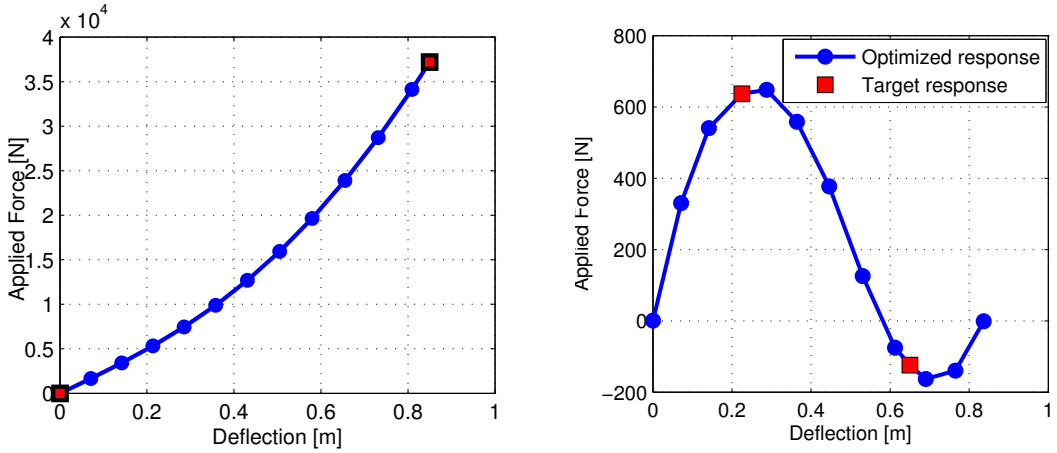

(a) Baseline beam

(b) Optimized bi-stable beam

Figure 7: Force-displacement plots for the baseline and optimized beam structures

4.2. Stent Examples

4.2.1. Stent Geometry and the Transverse Bracing System

For the design of a bi-stable stent, we isolate a single unit cell in the repeating mesh pattern and optimize the material layout within the cell to create a bi-stable effect. Using an approach similar to that which was implemented by Guimarães *et al.*[1] we model the unit cell as a two-dimensional planar structure. Figure 8 shows how the individual cells combine to form a cylindrical mesh structure. Note that in the local cell coordinates, the x-axis

coincides with the axial (z) dimension, while the y-axis corresponds to the circumferential direction (i.e. $y = \alpha r_0$, where r_0 is the radius of the cylinder).

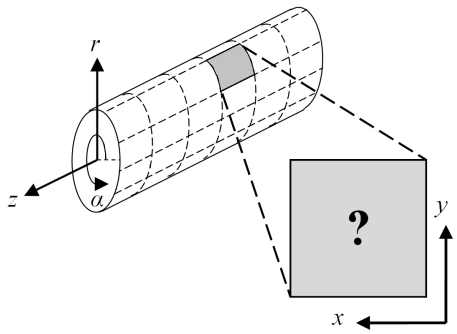

Figure 8: The two-dimensional design domain within the cylindrical stent structure

The cell interfaces (i.e. the domain along which adjacent unit cells are connected) are simulated using structural boundary conditions. Figure 9 shows the design domain and boundary conditions used in the layout design problem. Note that in the diagram, the support at point B, and the applied traction at point A, combine to form an expansion force exerted in the circumferential direction, y. The supports and tractions at points A, B, C, and D, represent junction points at which the cell is connected to adjacent cells. It is assumed that all portions of the boundary, which are not subject to tractions or fixed boundary conditions will be void of material in the optimized design. The selection of the locations of these junction points is a design choice that will impact the final structure produced by the algorithm.

As indicated in the figure, the length of the stent cell in the circumferential direction is 0.6mm. If we assume that the full circumference of the stent is 10 cells around, this corresponds to a diameter of roughly 1.9mm when the stent is in its contracted configuration. If we assume an expansion ratio of $1.5 \sim 2.0$, then this figure is consistent with other studies related to cardiovascular stents that assume a target blood vessel diameter of $2.5 \sim 4.0$mm [39]. The stent is assumed to be fabricated using a stiff biocompatible polymer, with a Young's modulus of $E = 3$GPa, and a Poisson's ratio of $\nu = 0.27$. This is in contrast to other common materials used in stents, such as stainless steel, which is highly ductile, and unlikely to exhibit the necessary elasticity required to achieve snap-though. Similarly, the other commonly used material, cobalt-chromium, is relatively brittle and unlikely to be able to withstand large deformations.

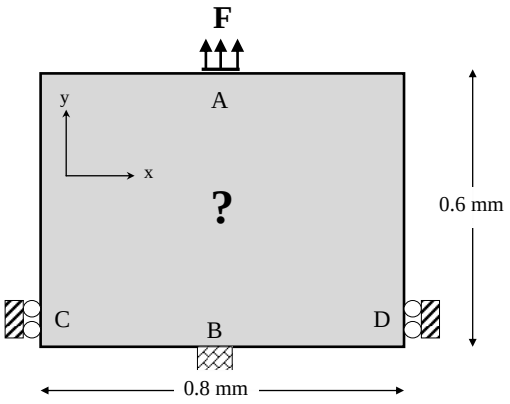

Figure 9: Design domain and boundary conditions for the stent layout design problem (the thickness in the radial direction is 0.05mm)

From the beam example, we see that one of the key factors required to achieve snap-through is the presence of a containing force that acts in the axial direction and prevents the beam from expanding outward. In the case of the beam example, this containing force is provided by the fixed clamp supports on the side of the beam. An analogous set of supports is also required for the stent structure. Therefore, these supports are included at points C and D in Fig. 9. Because there is no wall, or floor to which we can anchor the stent, we have devised a transverse bracing system, which comprises a series of nearly rigid stringers that line the surface of the stent in the axial direction. The stringers rest beneath the surface of the stent and are attached to the stent cells only at the points C and D. As the structural members of the stent mesh move into their expanded configuration, the lengths of the stringers remain fixed. Also, during the snap-through process, as the stent cells attempt to expand outward in the axial direction, they exert an outward force on the stringers that acts in the tensile direction along the stringers' axis. In turn, the stringers exert a reaction force, which counteracts and prevents that expansion. The stringers are assumed to be significantly stiffer than the stent cells in the axial direction, therefore the junction at which the stringers connect with the stent cells is treated as a fixed support in the topology optimization problem. Figure 10 shows the positioning of the stringers in relation to the stent geometry.

In addition to providing the containment force required to achieve snap-through, the transverse bracing system has two additional benefits. They

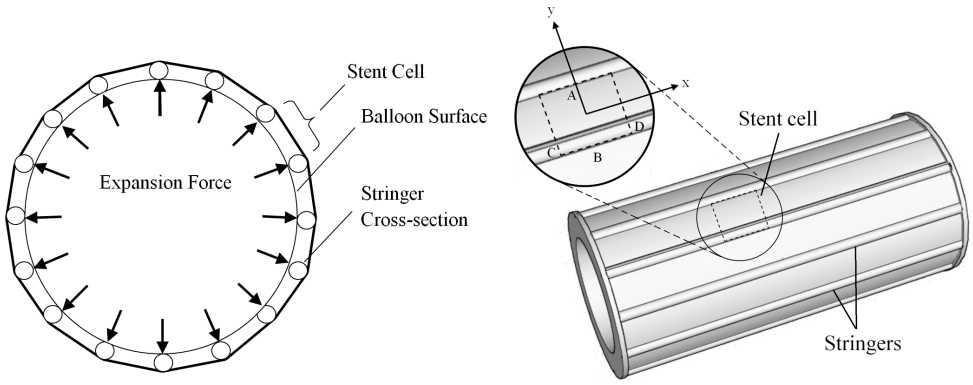

Figure 10: The transverse bracing system

provide a set of discrete contact points through which the expanding force from the balloon is transmitted to the stent mesh. Because the balloon makes contact with the stent only through the stringers, which remain fixed with respect to the balloon surface, the expansion process is frictionless and the stent cell will experience a purely planar tensile force in the circumferential direction. Figure 11 shows a free body diagram of all forces acting on the stent cell to demonstrate how they result in a two-dimensional plane stress problem.

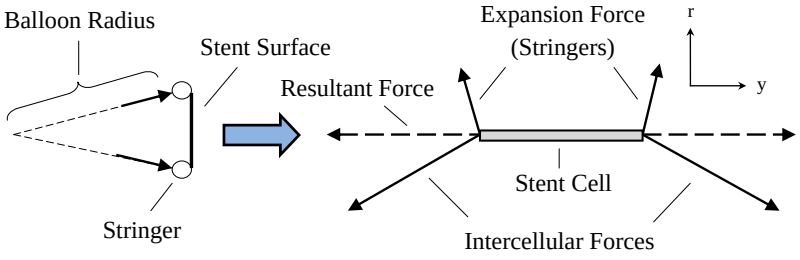

Figure 11: All forces acting on the stent cell, including expansion forces applied by the stringers, and tensile forces applied by adjacent cells

The second advantage of the transverse bracing system and the snap-through design concept is that, like the bi-stable beam, the bi-stable stent has a fixed length. This is highly advantageous because, as Tambaca *et al.* [3] observed, large changes in stent length, along with a lack of radial stiffness

and lack of bending flexibility, is a significant contributor to stent failure. Since the stringers need to be stiff only in tension, they can be fabricated using a woven, rope-like design, which would provide a high degree of bending flexibility, while maintaining tensile stiffness.

When the nonlinear structural analysis is initially performed for the baseline structure, in which the full rectangular domain is populated with material, the structure will have a tendency to contract in the horizontal direction, due to Poisson's ratio effects. The roller supports at points C and D will prevent this contraction by exerting an outward tensile force. However, we know that in the optimal stent design, the side supports must exert an inward compressive force if snap-through is to take place. Therefore, for the stent optimization problem, we enforce an additional constraint in which we require a reversal of direction in the reaction forces at the side supports. It is assumed that the solution for the optimal stent is symmetric, and so we include only the right half of the domain in the optimization problem. Therefore, the initial reaction force at support D exerted on the baseline structure is a pulling force exerted in the positive direction. To achieve snap-through, we apply a constraint on the reaction force, F_r, such that $F_r \leq -F_c$, where F_c is some small positive bound.

4.2.2. Numerical Results

The layout design problem shown in Fig. 9, was solved using the topology optimization procedure outlined above to obtain a bi-stable structure within the stent cell. The designated displacement points at which the constraint and objective forces are evaluated were set to $u_1 = 0.125$mm and $u_2 = 0.3$mm. The volume of the stent was constrained so that the design of the stent cell would occupy no more than 35% of the total area of the design domain. As in the bi-stable beam example, this volume constraint is chosen so that the optimizer eliminates superfluous material, without overly constraining the optimization. The force limit at displacement point 1 was set to $\theta_1 \geq 0.46$N. The containing force at each of the side supports was chosen as $F_c = 0.24$N. Figure 12 shows the optimized material layout for this particular design problem. Figure 13 shows the same stent structure from Fig. 12(a) in its expanded configuration. Also shown is the finite element mesh corresponding to the expanded displacement field.

As shown in Fig. 13(b), the mesh undergoes significant distortion due to the expansion process. This mesh distortion prevents us from reducing the material density (i.e. stiffness) beyond its prescribed minimum value

Figure 12: Optimized material layout for the unit cell of a bi-stable stent

(a) Expanded structure

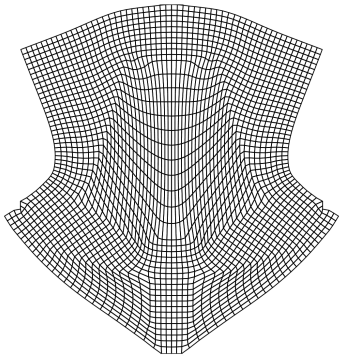

(b) Deformed mesh

Figure 13: Stent structure in its expanded position

of $\rho_{\min} = 2.5^{-3}$, as this would lead to the creation of degenerate elements. Moreover, the presence of non-zero stiffness elements in this void region contributes some stiffness to the structure and prevents us from accurately predicting the force-displacement response of the design. Therefore, to obtain a more accurate picture of the design's true force-displacement curve, we have implemented an algorithm that removes all void and nearly void elements from the finite element mesh, along with their respective degrees of freedom. We then generate a new force-displacement curve by performing a nonlinear finite element analysis using the reduced mesh. Figure 14 shows the reduced mesh corresponding to the optimized design shown in Fig. 12 in both the initial and deformed states. The threshold for element removal was chosen as $\rho_{\text{remove}} = 0.1$.

Figure 15 shows the force-displacement plots for the baseline structure (i.e. a uniform structure in which all elements have full material density), as well as for the optimized structure analyzed using both the full and reduced

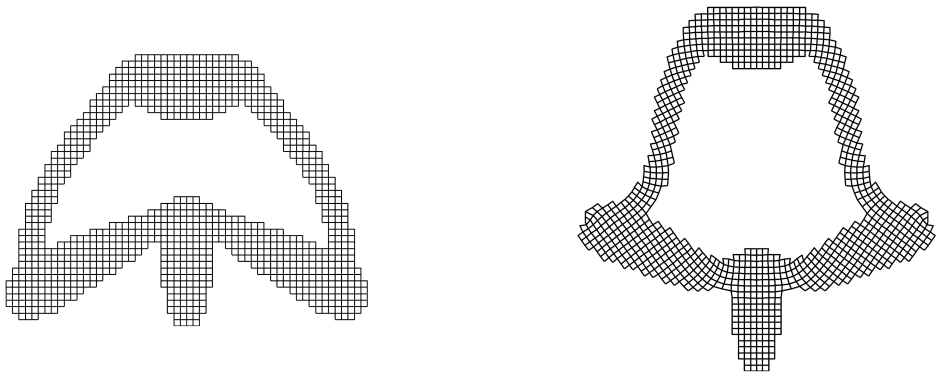

(a) Undeformed mesh (b) Deformed mesh

Figure 14: Reduced mesh for the bi-stable stent cell structure

meshes. Similar to the bar example, the force-displacement path of the baseline structure is monotonic, however by redistributing material within the domain, we are able to tailor the structural response to achieve the multimodal curve that characterizes snap-through. The plot indicates that prior to the removal of void elements from the finite element mesh, the structure does not appear to be bi-stable since the applied force remains positive throughout the expansion process. However, when the void elements are removed, the resulting analysis reveals that the optimized structure is indeed bi-stable, and its secondary (expanded) stable position occurs at a displacement of 0.249mm. This corresponds to an expansion ratio of approximately 1.415, and an expanded diameter of roughly 2.67mm. Note that Figs. 13 and 14(b) correspond to the stable equilibrium displacement, $u = 0.249$mm.

To attempt to improve upon the above design and achieve a larger expansion ratio, we have implemented the design optimization algorithm using an alternative set of boundary conditions. Figure 16, shows the design domain and boundary conditions, along with the optimized material layout for the alternative stent design. Note that in this problem, as well as in the previous examples, we exploit all symmetry. Using this strategy, the structure shown in Fig. 16 becomes fixed via roller supports along its horizontal and vertical lines of symmetry. As in the previous problem, the applied forces at points A and B, are generated by the connection to adjacent cells within the stent mesh. The roller supports at points C, D, E, and F represent junctions at which the stent cell connects to adjacent cells and where the cell is supported in the x direction by the stringers.

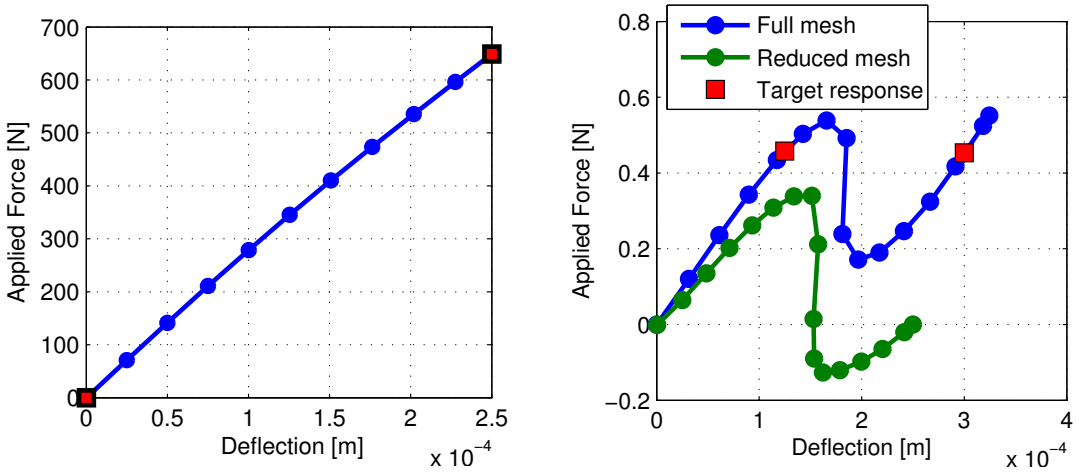

(a) Baseline structure (b) Optimized structure

Figure 15: Force-displacement response of the bi-stable stent structure during the expansion process

The designated displacement points were set to $u_1 = 0.1$mm and $u_2 = 0.25$mm measured from the horizontal axis of symmetry. The stiffness constraint was set to $\theta_1 \geq 0.68$N, and the containing force bound was set to $F_c = 0.20$N. For this problem, we enforce an additional constraint on the vertical displacement at the side supports. Since we are designing only the top right quadrant of the domain, this can be achieved with a single constraint such that $u_D \leq 0.01$mm. Although the constraint ends up being inactive in the converged solution, this step allows us to avoid local minima in which the optimizer seeks to reduce the applied force θ_2 by simply removing or weakening the connection between the upper and lower side supports.

From the optimized material layout we can clearly identify narrow regions in the structure, which act as flexural hinges, and about which rotational motion takes place. Away from these regions, the strain values tend to be relatively low. Figure 17 shows the optimized stent structure in its expanded configuration, along with the corresponding finite element mesh. Here again, we see high levels of mesh distortion is the region enclosed by the stent structure.

As in the previous example, to obtain a more accurate representation of the force-displacement response of the optimized design, we removed all void elements, and performed an additional structural analysis using the resulting

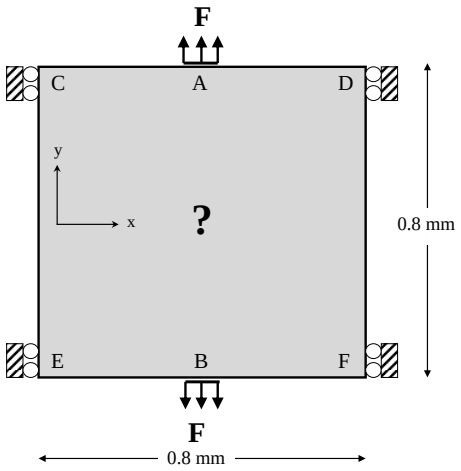

(a) Design domain and boundary conditions

(b) Optimized material distribution

Figure 16: The alternative stent design problem

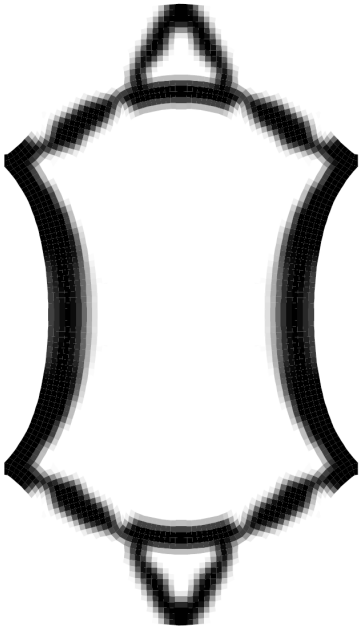

(a) Expanded structure

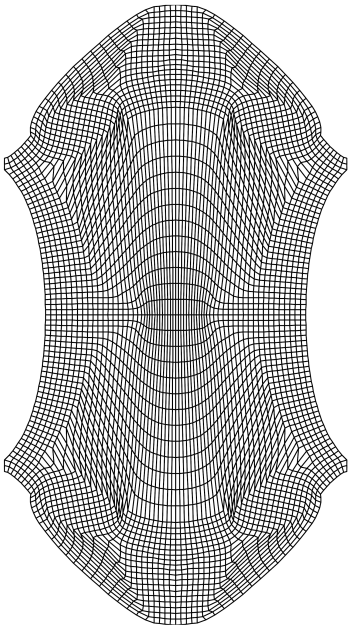

(b) Deformed mesh

Figure 17: Alternative stent structure in its expanded position

mesh. Figure 18 shows the reduced mesh corresponding to the optimized material layout in both the stressed and unstressed stable configurations. Figure 19 shows the force-displacement plots for the baseline structure, as well as plots for the optimized structure obtained using the full and reduced finite element mesh. Note that based on the analysis performed using the full mesh, the algorithm is able to push the force-displacement curve down significantly beyond the monotonically increasing path associated with the baseline structure. However, it is only after we remove the void elements from the analysis that we are able to fully capture the bi-stable behavior of the optimized design. In this case, the design reaches it secondary stable configuration once the displacement reaches 0.308mm from either side of the horizontal symmetry axis. This corresponds to an expansion ratio of 1.770.

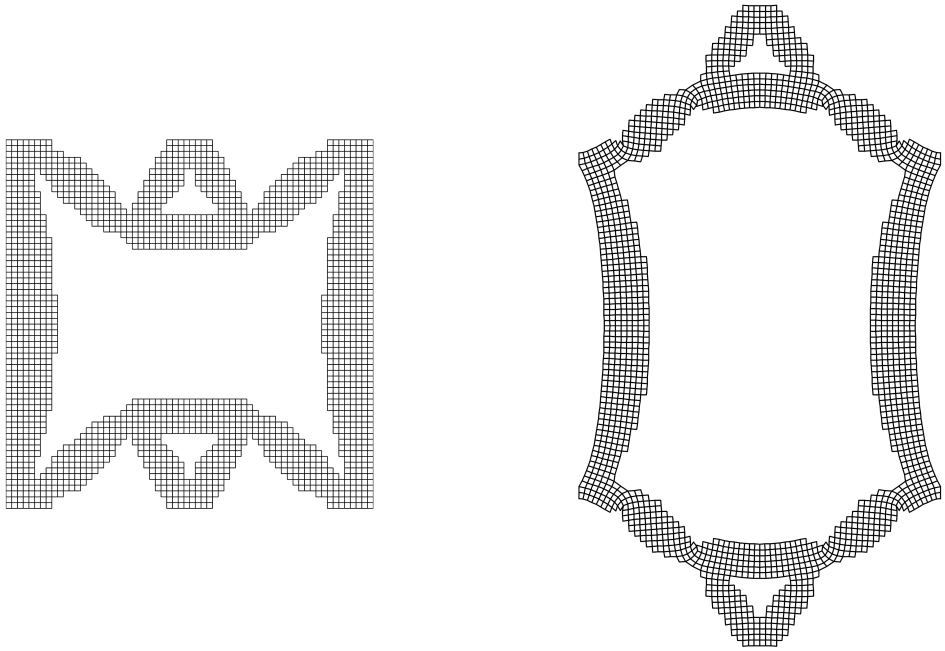

(a) Undeformed Mesh (b) Deformed mesh

Figure 18: Reduced finite element mesh for the alternative stent design

Figures 20 and 21, show the cellular mesh patterns corresponding to the original and alternative bi-stable stent designs in both the contracted and expanded configurations . The green lines indicate the locations of the stringers within the stent structure, and the red dots represent the junction points at which the stringers are joined to the stent mesh. For completion, we have

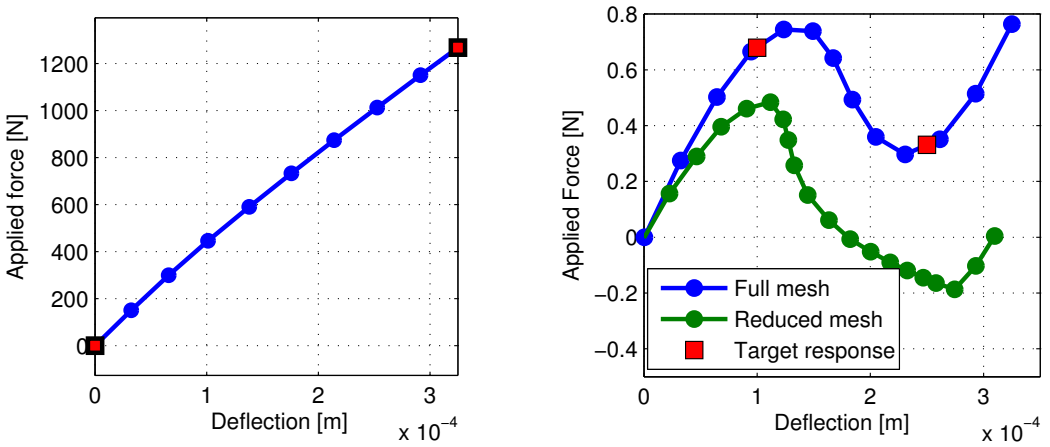

(a) Baseline structure

(b) Optimized structure

Figure 19: Force-displacement plots for the baseline and optimized structures corresponding to the alternative stent design problem shown in Fig. 16

also provided the convergence plot showing the evolution of the objective and constraint function (θ_2 and θ_1) respectively for the optimization of the alternative stent design (see Fig. 22). Note that that while the force value for θ_2 is reduced significantly over the course of the optimization, it never achieves a negative value. This is because the optimization algorithm uses analysis based only on the full finite element mesh, in which void elements and their degrees of freedom are included in the finite element mesh.

The mesh layouts shown in Figs. 20 and 21 can be manufactured relatively easily using current additive manufacturing techniques. However, some post-processing is necessary to obtain a manufacturable design. This includes the task of obtaining a sharp, well-defined material boundary. There exist several well-established techniques for achieving well-defined boundaries in element-based topology optimization schemes, such as mesh refinement [40], thresholding [32] and projection methods [41], all of which are fully compatible with the optimization process described above. Future work will be devoted to investigating manufacturing considerations and further understanding how manufacturability will impact the design task.

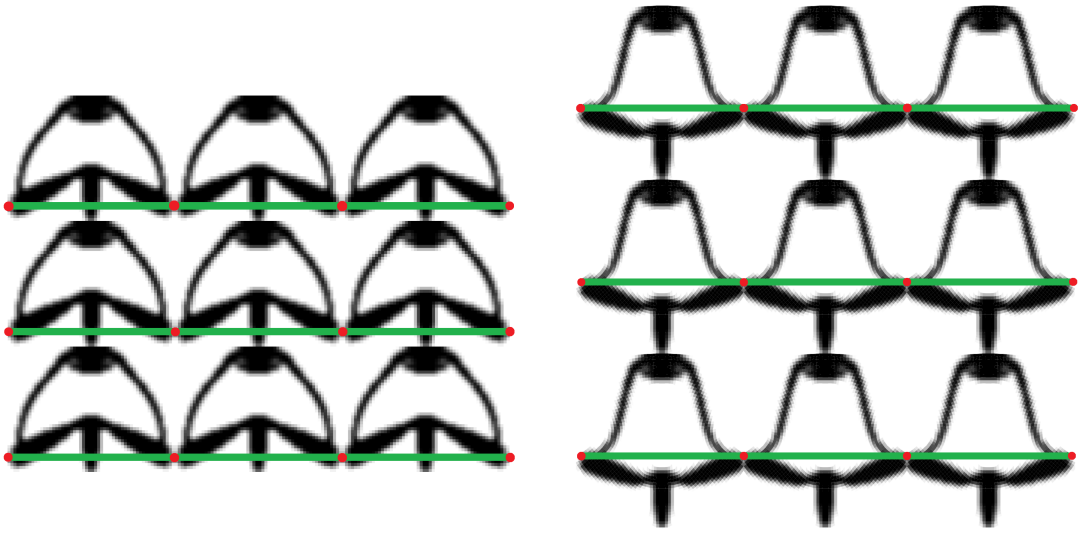

(a) Unstressed configuration (b) Expanded configuration

Figure 20: Optimized bi-stable mesh patterns for the original stent design

5. Conclusions

We have proposed an original design concept for a bi-stable cardiovascular stent. The material layout of the cellular mesh structure was generated using a topology optimization framework with a Neo-Hookean, hyperelastic finite element model being used to perform the forward analysis. Adjoint sensitivity analysis was used to accurately and efficiently evaluate the gradients of the structural response. In order to generate the containing force required to achieve snap-through and bi-stability, we proposed a transverse bracing system comprising a series of stringers lining the inside of the mesh along the axial direction. Through optimization, we were able to tailor the nonlinear response of the stent structure to produce a design that exhibited the desired snap-through effect. The algorithm was used to create two different designs for the stent cell, using two different sets of boundary conditions. When the the elements from the void region were removed from the finite element mesh, a subsequent analysis revealed that both structures were indeed bi-stable. Results showed that the two design reached fully stable secondary equilibrium states with expansion ratios of 1.415 and 1.770. This result is significant since it provides an alternative mechanism through which to reliably achieve complete expansion by exploiting the geometric nonlinearity of

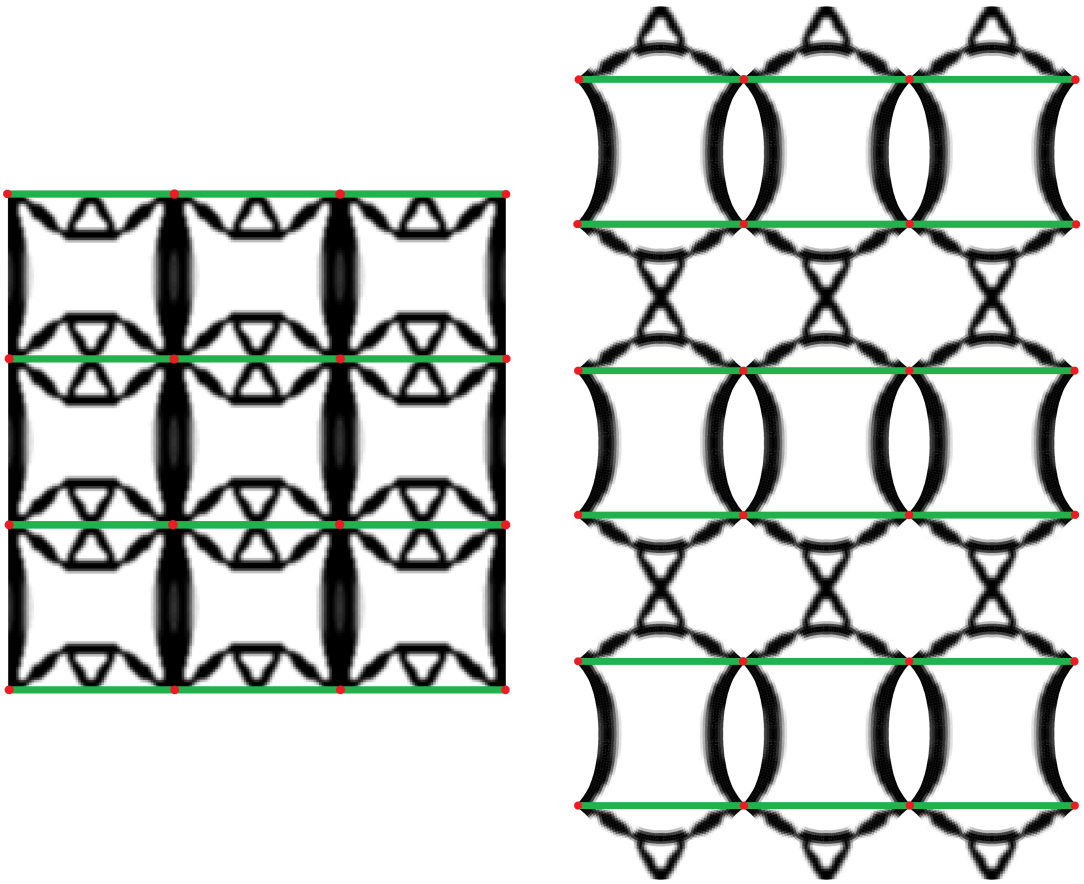

(a) Unstressed configuration (b) Expanded configuration

Figure 21: Optimized bi-stable mesh patterns for the alternative stent design

the structure. Furthermore, the highly controlled expansion process allows for an expanded stent that is fully uniform along its length. Lastly, the combination of the transverse bracing system along with snap-through, ensures that the length of the device remains constant throughout the expansion process. Future work will include full three-dimensional simulation of the stent designs, to investigate the impact of 3D effects. Additionally, ongoing experimental work will be aimed at prototyping and testing the 3D stent designs. For future work we will also investigate the implementation of additional objective functions and design constraints that address considerations such as hemodynamic performance as well as recoil and tissue interaction.

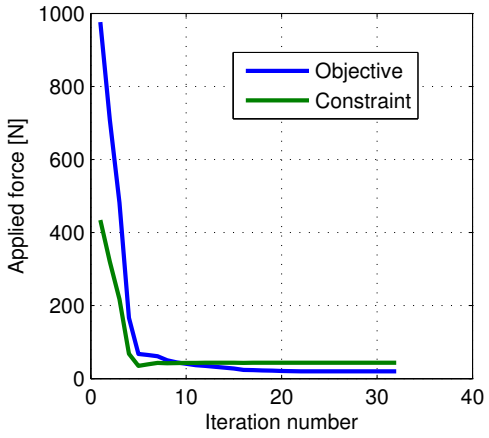

Figure 22: Convergence histories of the objective and constraint functions for the optimization of the alternative stent design

Acknowledgements

This research was supported by the National Science Foundation's Division of Civil, Mechanical and Manufacturing Innovation under grant number CMMI-1334857.

References

[1] T. Guimarães, S. Oliveira, M. Cuarte, Application of the topological optimization technique to the stents cells design for angioplasty, J. Braz. Soc. of Mech. Sci. & Eng. 30 (3) (2009) 261–268.

[2] S. Pant, G. Limbert, N. Curzen, N. Bressloff, Multiobjective design optimisation of coronary stents, Biomaterials 32 (31) (2011) 7755–7773.

[3] J. Tambaca, S. Canic, M. Kosor, R. Fish, D. Paniagua, Mechanical behavior of fully expanded commercially available endovascular coronary stents, Texas Heart Institute Journal 38 (5) (2011) 491–501.

[4] H. Li, T. Qiu, B. Zhu, J. Wu, X. Wang, Design optimization of coronary stent based on finite element models, The Scientific World Journal 2013 (2013) 1–10.

[5] E. Nokolsky, L. Gruberg, S. Pechersky, M. Kapeliovich, E. Grenadier, S. Amikam, M. B. M. Suleiman, W. Markiewicz, R. Beyar, Stent deployment failure: reasons, implications, and short- and long-term outcomes, Catheter Cardiovasc Interv. 59 (3) (2008) 324–328.

[6] D. Beule, P. Mortier, S. Carlier, B. Verhegghe, R. V. Impe, Realistic finite element-based stent design: The impact of balloon folding, Journal of Biomechanics 41 (2) (2008) 383–389.

[7] S. Chua, B. MacDonald, M. Hashmi, Finite element simulation of stent expansion, Journal of Materials Processing Technology 120 (1-3) (2002) 335–340.

[8] S. Chua, B. MacDonald, M. Hashmi, Increased risk of restenosis after placement of gold-coated stents: results of a randomized trial comparing gold-coated with uncoated steel stents in patients with coronary artery disease, Circulation 101 (21) (2000) 2478–2483.

[9] C. Rogers, D. Tseng, J. Squire, E. Edelman, Balloon-artery interactions during stent placement: a finite element analysis approach to pressure, compliance, and stent design as contributors to vascular injury, Circ. Res. 84 (4) (1999) 378–383.

[10] T. Gundert, A. Marsden, W. Yang, J. L. Jr., Optimization of cardiovascular stent design using computational fluid dynamics, Journal of Biomechanical Engineering 134 (1) (2012) 1–8.

[11] D. Yang, B. Mosadegh, A. Ainla, B. Lee, F. Khashai, Z. Shuo, K. Bertoldi, G. Whitesides, Buckling of elastomeric beams enables actuation of soft machines, Advanced Materials.

[12] S. Rudykh, Snap-through actuationofthick-wallelectroactiveballoons, International Journal of Non-linear Mechanics 47 (2012) 206–209.

[13] J. Overvelde, T. Kloek, J. D'haen, K. Bertoldi, Amplifying the response of soft actuators by harnessing snap-through instabilities, PNAS.

[14] T. E. Bruns, D. A. Tortorelli, Topology optimization of non-linear elastic structures and compliant mechanisms, Comput. Method Appl. Mech. Eng. 190 (26-27) (2001) 3443–3459.

[15] M. Frecker, N. Kikuchi, S. Kota, Topology optimization of compliant mechanisms with multiple outputs, Struct. Opt. 17 (1999) 269–278.

[16] M. Frecker, G. Ananthasuresh, N. Nishiwaki, N. Kikuchi, S. Kota, Topological synthesis of compliant mechanisms using multicriteria optimization, ASME J. Mech. Des. 119 (1-3) (1997) 238–245.

[17] O. Sigmund, On the design of compliant mechanisms using topology optimization, Mechanics of Structures and Machines 25 (4) (1997) 493–524.

[18] O. Sigmund, S. Torquato, Design of smart composite materials using topology optimization, Smart. Mater. Struct. 8 (1999) 365–379.

[19] U. Larsen, O. Sigmund, S. Bouwstra, Design and fabrication of compliant micromechanisms and structures with negative poissons ratio, Journal of Microelectromechanical Systems 6 (2) (1997) 99–106.

[20] A. R. Jr., G. Paulino, Convex topology optimization for hyperelastic trusses based on the ground-structure approach, Structural and Multidisciplinary Optimization 51 (2) (2015) 287–304.

[21] M. Wallin, M. Ristinmaa, Finite strain topology optimization based on phase-field regularization, Struct. Multidisc. Optim. 51 (2) (2014) 305–317.

[22] F. Wang, B. Lazarov, O. Sigmund, J. Jensen, Interpolation scheme for fictitious domain techniques and topology optimization of finite strain elastic problems, Computer Methods in Applied Mechanics and Engineering 276 (2014) 453–472.

[23] T. Bruns, O. Sigmund, D. Tortorelli, Numerical methods for the topology optimization of structures that exhibit snap-through, Int. J. Numer. Meth. Engng. 55 (2002) 1215–1237.

[24] E. Lindgaard, J. Dahl, On compliance and buckling objective functions in topology optimization of snap-through problems, Struct. Multidisc. Optim. 47 (2013) 409–421.

[25] T. Belytschko, W. Liu, B. Moran, Nonlinear Finite Elements for Continua and Structures, Wiley, Chichester, West Sussex, UK, 2000.

[26] P. Wriggers, Nonlinear Finite Element Methods, Springer, New York, NY, 2008.

[27] M. Zhou, G. I. N. Rozvany, The COC algorithm, part II: Topological, geometrical and generalized shape optimization, Int. J. Numer. Meth. Engrg. 37 (1991) 2471–2499.

[28] M. P. Bendsøe, Optimal shape design as a material distribution problem, Struct. Optim. 1 (1989) 193–202.

[29] O. Sigmund, J. Peterson, Numerical instabilities in topology optimization: A survey on procedures dealing with checkerboards, mesh-dependencies and local minima, Struct. Optim. 16 (1998) 68–75.

[30] C. S. Jog, R. B. Haber, Stability of finite element models for distributed parameter optimization and topology design, Comput. Meth. Appl. Mech. Engrg. 130 (1996) 203–226.

[31] C. Le, J. Norato, T. Bruns, C. Ha, D. Tortorelli, Stress-based topology optimization for continua, Struct. Multidisc. Optim. 41 (2010) 605–620.

[32] O. Sigmund, On the usefulness of non-gradient approaches in topology optimization, Structural and Multidisciplinary Optimization 43 (5) (2011) 589–596.

[33] C. A. Mader, J. R. R. A. Martins, J. J. Alonso, E. van der Weide, Adjoint: An approach for the rapid development of discrete adjoint solvers, AIAA J. 46 (2008) 863–873.

[34] J. R. R. A. Martins, J. J. Alonso, J. J. Reuther, A coupled-adjoint sensitivity analysis method for high-fidelity aero-structural design, Optim. Engrg. 6 (2005) 33–62.

[35] K. Svanberg, The method of moving asymptotes - a new method for structural optimization, Int. J. Numer. Meth. Optim. 24 (1987) 359–373.

[36] H. Kuhn, A. Tucker, Nonlinear programming, in: Proceedings of 2nd Berkeley Symposium, Berkeley, CA, 1951.

[37] W. Karush, Minima of functions of several variables with inequalities as side constraints, Master's thesis, University of Chicago, Chicago, IL (1939).

[38] G. Allaire, G. Francourt, A numerical algorithm for topology and shape optimization, in: Topology Design of Structures, Kluwer, Dorcrecht, 1993.

[39] J. Hagemeister, F. Baer, R. Schwinger, H. Höpp, Compliance of a cobalt chromium coronary stent alloy the COVIS trial, Curr. Control Trials Cardiovasc. Med. 6 (1) (2005) 1–4.

[40] K. Maute, E. Ramm, Adaptive topology optimization, Struct. Optim 10 (2) (1995) 100–112.

[41] J. Guest, J. Prevost, T. Belytschko, Achieving minimum length scale in topology optimization using nodal design variables and projection functions, Int. J. Numer. Meth. Engrng. 61 (2) (2004) 238–254.